# Modeling ice melt rates from seawater intrusions in the grounding zone of Petermann Gletscher, Greenland

**R. Gadi[1], E.Rignot[1,2,3], D.Menemenlis[2]**

[1]University of California Irvine, Department of Earth System Science, Irvine CA 92697
[2]Jet Propulsion Laboratory, California Institute of Technology, 4800 Oak Grove Drive, Pasadena, CA 91109
[3]University of California Irvine, Department of Civil and Environmental Engineering, Irvine CA 92697

**Key Points:**

- First modeling of ice melt rates from seawater intrusions in the kilometer-size grounding zone of Petermann Glacier using an ocean model.
- Modeled melt rates are highest in the grounding zone and increase linearly with grounding zone width and ocean thermal forcing.
- High melt rates in kilometer-size grounding zones imply a higher sensitivity of glaciers to ocean warming than anticipated.

Corresponding author: Ratnakar Gadi, rgadi@uci.edu

## Abstract

Satellite radar interferometry data reveals that the grounding line of Petermann Glacier, Greenland migrates by several kilometers during the tidal cycle, bringing pressurized, subsurface, warm ocean waters in regular contact with a large sector of grounded ice. We use the Massachusetts Institute of Technology general circulation model in two dimensions to calculate the ice melt rates as a function of grounding zone width and ocean thermal forcing. Ice melt rates are found to be higher in the grounding zone cavity than anywhere else in the ice shelf cavity. The melt rates increase sub-linearly with the width of the grounding zone and ocean thermal forcing. The model results agree well with remote sensing estimates of ice melt. High basal ice melt rates in tidally-flushed grounding zones imply that marine-terminating glaciers are more sensitive to ocean thermal forcing than anticipated, which will increase their projected contribution to sea level rise.



## Plain Language Summary

The traditional view of ice melting in contact with ocean waters is that melt rates drop to zero at the grounding line, which is a semi-fixed boundary at the junction between grounded ice and the ocean. In reality, the grounding line migrates by kilometers during the tidal cycle, more than ten times beyond the range expected from hydrostatic equilibrium, which brings warm, saline water in rapid contact with broad sectors of grounded ice. We use an ocean model to calculate the melt rates caused by seawater intrusions. We find that the melt rates in the grounding zone are higher than anywhere else in the ice shelf cavity and increase as the grounding zone becomes wider and the ocean gets warmer. Ice melt in kilometer-size grounding zones will reduce the basal resistance to flow and will increase the sensitivity of the glacier flow to ocean warming, hence projections of sea level rise from the glacier will go up.


## 1 Introduction

Petermann Glacier is a major outlet glacier in North Greenland located at 60°W, 81°N. The glacier forms a 20-km wide and 45-km long floating ice shelf, which is the second longest floating ice tongue in the northern hemisphere (Figure 1a). Petermann drains 4% of the Greenland Ice Sheet in area (Mouginot et al., 2019). Ice discharge across the grounding line is ten times larger than the sum of surface melt and iceberg calving. This partitioning in mass loss has been explained by high melt rates of the ice shelf base in contact with warm ocean waters (Rignot & Steffen, 2008). Following a period of stability in the 20th century, Petermann Ice Shelf was affected by two major calving events in 2010 and 2012, which shortened its length by 25 km (Johannessen et al., 2013; Nick et al., 2012; Münchow et al., 2014). Around 2018, the glacier grounding line started to retreat by 7 kilometers at the center, 4 km on the sides, and the glacier had sped up by about 100 - 150 m/yr in 2022 (Millan et al., 2022).

The traditional view of a glacier grounding line is that it migrates over short distances, i.e. typically less than one unit model element, or 100-200 m, based on maintaining hydrostatic equilibrium during the tidal cycle; and ice melt rates converge to zero at the mean sea level grounding line. For instance, for a glacier slope of 1%, the grounding line should migrate by 100 m in response to a 1-m tide. Dense time series of satellite radar interferometry data, however, reveals that the grounding line migrates by several kilometers during the tidal cycle (Ciraci et al., 2023) (Fig. 1b). Such a high level of migration is not accounted for in ice sheet models or in models of ice-ocean interaction. The migration reveals kilometer-size seawater intrusions which have the potential to bring ocean heat at a rapid rate in contact with ice and hence melt it vigorously (Jenkins, 1991; Walker et al., 2013; Sayag & Worster, 2013). If the ocean waters get warmer, the intrusions will bring more heat in contact with grounded ice, over considerable distances,

reducing basal resistance to glacier flow, which in turn will lead to glacier speed up and cause a larger contribution to sea level rise from the glacier.

The grounding zone quoted herein is not the same as the flexure zone (Brunt et al., 2010). The flexure zone is a region about 5-10-km wide where the glacier progressively adjusts to hydrostatic equilibrium downstream of the grounding line. The grounding line is the location where ice detaches from the bed for the first time. The grounding zone delineates the region of migration of the grounding line itself, which is equivalent to the migration of the inland limit of flexure. Until recently, it was thought that the grounding zone was narrow and therefore equivalent to a line. We have, however, now evidence for kilometer-size grounding zones.

The magnitude of ice melt in the grounding zone is not well known. Recent estimates from a time series of digital elevation models and ice velocity from remote sensing, and reconstruction of surface balance from climate models suggest that the melt rates are high in the grounding zone (40-80 m/yr) and higher than anywhere else in the ice shelf cavity (Ciraci et al., 2023). If these observations are correct, seawater intrusions will have a considerable impact on glacier stability and evolution.

Earlier modeling studies, which did not have direct evidence for seawater intrusions, suggested that including such intrusions in models could up to double the projections of mass loss in a warming climate (Walker et al., 2013; Parizek et al., 2013), which was confirmed by more recent studies (Seroussi & Morlighem, 2018; Robel et al., 2022). Other studies have also proposed physical mechanisms for seawater intrusions over kilometer-scale distances (Wilson et al., 2020).

Here, we employ a two-dimensional configuration of the Massachusetts Institute of Technology global circulation model (MITgcm) ocean model, with bathymetry, ice shelf thickness, ocean thermal forcing, and tidal motion. We model ice-ocean interactions in a narrow, time-varying grounding zone inferred from satellite data. We model the ice melt rates and their sensitivity to: 1) oceanic Thermal Forcing (TF) and 2) the grounding zone width. We compare our model results with satellite-derived estimates of ice melt. We parameterize the modeled ice melt as a function of thermal forcing and distance of the seawater intrusions. We conclude on the impact of the model results on projections of sea level rise from Petermann and other marine-terminating glaciers.

## 2 Data and Methods

*Tidal motion of the ice shelf.* We measure tidal motion with Interferometric Synthetic Aperture Radar (InSAR) data from the Earth Remote Sensing satellite -1 (ERS-1), Sentinel-1, CosmoSkyMed, and ICEYE (Millan et al., 2022; Ciraci et al., 2023). We distinguish three regions of vertical ice motion (Fig. 1b): 1) The freely floating ice shelf, which experiences a vertical motion nearly in phase with the oceanic tide (Reeh et al., 2003) and of the same exact amplitude; 2) a flexure zone (FZ), which experiences a vertical tidal motion that decreases linearly with distance from the freely floating ice shelf and reaches zero at the grounding line; and 3) a zone of migration of the grounding line during the tidal cycle, or grounding zone (GZ). If the grounding line is fixed in time, the grounding zone is less than one model element. Here, the grounding zone width varies from 1 to 6 km (Ciraci et al., 2023). Within the grounding zone, the vertical motion of the ice measured with radar interferometry is similar to that recorded in a flexure zone, i.e., less than the tidal amplitude and typically a few centimeters to a few tens of centimeters. The vertical motion of the ice is caused by water intrusions of the same order magnitude height (i.e., could be freshwater or seawater).

*Model Domain.* We select a two-dimensional (2D) section along the center line of Petermann Glacier (Fig. 1c). Bathymetry is from a three-dimensional (3D) inversion of high-resolution gravity data (An et al. (2019); Ciraci et al. (2023)). Ice thickness is de-

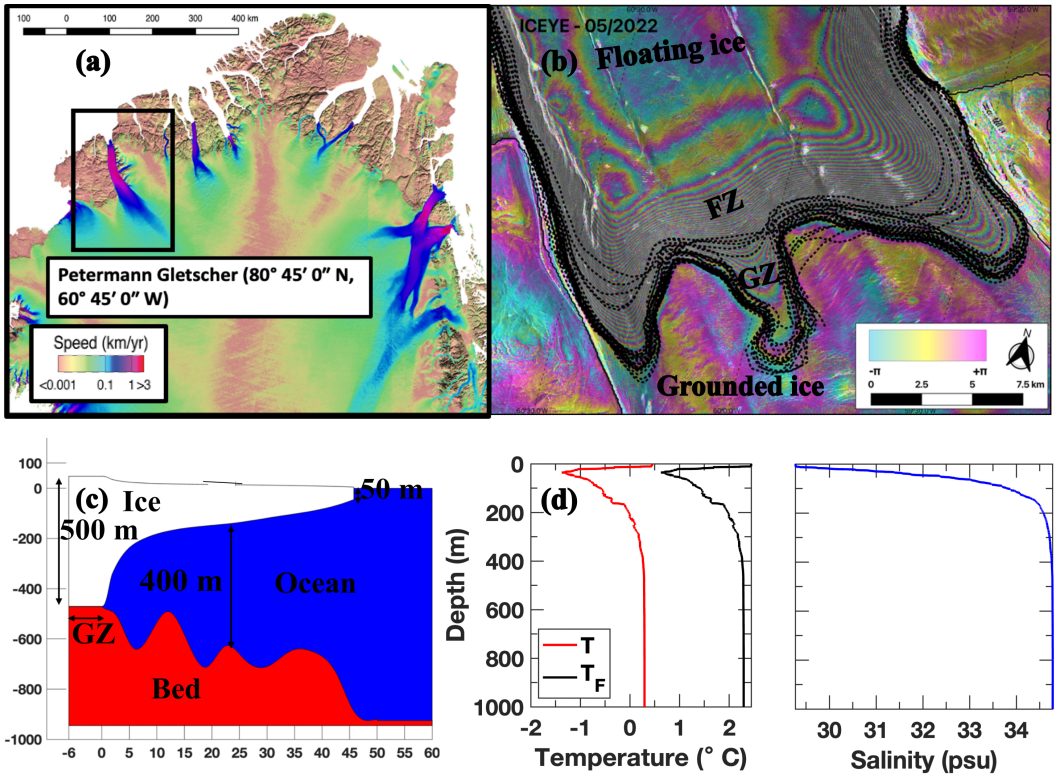


**Figure 1. Model domain for the grounding zone of Petermann Glacier**. (a) Location of Petermann Glacier in Greenland overlaid on a speed map color coded. (b) synthetic-aperture radar data observations of grounding line (thin black lines) migration at tidal frequencies overlaid on interferometric fringes (360° variations in phase; each fringe is a 1.3 cm incremental vertical displacement of the ice surface) of differential tidal motion from ICEYE. The zone of concentrated fringes is the flexure zone (FZ). The inner limit of the flexure zone is the grounding line. The zone of migration of the grounding line during the tidal cycle is the grounding zone (GZ). (c) two-dimensional cross-section of Petermann Glacier with ice (white), bed (red), and ocean water (blue). (d) Conductivity, Temperature, Depth (CTD) data from year 2015 (Jakobsson et al., 2018).

rived from a TANDEM-X digital elevation model (DEM) of the ice surface from year 2022 assuming hydrostatic equilibrium of the ice (Ciraci et al., 2023). The grounding zone cavity is a rectangular cavity of one vertical ocean element, i.e., 1 m here. We utilize a Cartesian grid with a vertical spacing of 1 m and a horizontal spacing ranging from 20 m in the grounding zone, linearly increasing to 500 m at the ice front.

The elevation of the ice-shelf base exhibits an inflection point at the cavity entrance. This break in slope has a strong influence on ice melt and, in particular, generates high melt rates. After evaluating various ways to "smooth out" this transition, we adopt the approach in Warburton et al. (2020).

*MITgcm Ocean model.* MITgcm employs a finite-volume grid point algorithm to solve the Boussinesq hydrostatic form of the Navier-Stokes equations for an incompressible fluid on an Arakawa C-grid (Marshall et al. (1997)). The MITgcm model incorporates the SHELFICE package, specifically designed to handle ice-shelf cavities (Losch (2008)). The model calculates melt rates and the corresponding heat and salt fluxes at

the ice-ocean interface, solving the three-element equations in (Holland and Jenkins (1999)). These heat and salt fluxes are determined using the velocity-dependent melt rate parameterization in Dansereau et al. (2014). We use the vertical re-meshing package in (Jordan et al. (2018)).

We incorporate the effects of ice bending and grounding line migration into the MITgcm model. Ice motion in the flexure zone starts from zero at the grounding line and linearly increases to the full tidal amplitude at the end of the flexure zone. Instead of forcing the ice shelf position as an input to the code, we change the mass of the ice shelf. Specifically, using the known deflection of ice between two timestamps, we multiply it by the density of ice to determine how to alter the ice shelf mass. This methodology is employed because MITgcm uses the weight of the ice shelf as a boundary condition. Tidal forcing is a sinusoidal function of amplitude $\pm 1$ m. In response to changes in oceanic tide, the grounding line migrates back and forth at a speed which is the ratio of the width of the grounding line divided by half of a tidal cycle, or 6 hours. For a cavity of 6 km, the speed of cavity opening is 28 cm/s.

The simulations use a time step of 1 second to ensure computational stability. We employ zero horizontal diffusivity, a vertical diffusivity of 2.8 $10^{-5}\mathrm{m}^2/\mathrm{s}$, horizontal viscosity of 0.3 $\mathrm{m}^2/\mathrm{s}$, vertical viscosity of 2.8 $10^{-4}\mathrm{m}^2/\mathrm{s}$, and bi-harmonic viscosity of 2.5 $m^4/s$. Salinity and temperature values are prescribed at the ocean boundary using Conductivity Temperature Depth (CTD) data collected in August 2015 (Jakobsson et al., 2018). To relax the model output to the boundary condition, we utilize a sponge layer with a length of approximately 5 km and a relaxation time of 1 day. Each experiment is conducted with a horizontally homogeneous temperature-salinity profile within the entire domain. We find that the simulations converge after two tidal cycles, i.e., the modeled results do not change at a detectable level (1 decimal) after two cycles.

*Experiments.* We conduct a series of simulations with a fixed grounding line where we adjust the ocean model parameters to match earlier simulations of ice melt by Cai et al. (2017). Secondly, we adjust the cavity length by increments of 1 km while maintaining the same ocean thermal forcing. The melt rate in the three-equation parameterization relies on the transfer coefficient for heat and salt, $\gamma_T$ and $\gamma_S$, and the mixed layer velocity, $U_m$, derived from the model. Thirdly, we conduct simulations where we adjust the thermal forcing in increments of 0.5°C, from 0.75°C to 3.25°C. To do so, we apply a uniform shift to the 2015 temperature profile. Thermal forcing is the deviation of the in-situ water temperature, $T_w$, from the depth-dependent, salinity-dependent, freezing point of seawater, $T_f$, i.e., $TF = T_w - T_f$. At the entrance of the grounding zone, we force the curvature of the ice shelf base to be proportional to $U_m^{2/5}$ as in (Warburton et al., 2020).

## 3 Results

*Melt pattern.* The tidally-average melt rate observed in our numerical simulations exhibits the general profile in Figure 2. The melt rate is highest at the cavity entrance, which is the position of the grounding line at low tide, and decreases to zero toward the termination of the cavity. Outside the cavity, the melt rate drops rapidly, then returns to high values within a few hundred meters, forms a secondary peak, and then decays slowly for the next 10-20 km, depending on thermal forcing. We find that the first tidal cycle produces higher melt rates than the second tidal cycle because the cavity initially fills with warm waters (Fig. S1). The melt rate varies with time in the cavity as a function of ocean state, water speed, and heat flux (Fig. S2). Starting in the second cycles, the cavity fills with a mix of warm seawater and residual melt water (Fig. S3), so the melt rates decrease slightly. The model converges in two cycles, i.e. the results do not change after two cycles.

The peak melt rate at the mouth of the grounding zone cavity varies from 30 m/yr with 1.25°C thermal forcing to 70 m/yr with 3.25 °C thermal forcing for a grounding zone width of 6 km (Fig. 2b). For comparison, the melt rate with no grounding zone peaks at a distance of 5 km from the grounding line to 15 m/yr with a 2.25°C thermal forcing, i.e. twice less than when a grounding zone of 6 km is present.

The melt rate decreases rapidly toward the termination of the grounding zone cavity and reaches zero well beyond the termination of the cavity, typically within the last kilometer. In the first cycle, the melt rates are higher in the termination of the cavity which fills with warm water (Fig. S3). When the cavity is flushed out for the first time, not all the water leaves the cavity, some melt water gets trapped. In the next cycle, seawater intrusions do not penetrate to the entire cavity. We find that seawater on average reaches about 72% of the cavity for different cavity lengths (Fig. S3). The remainder of the cavity is filled with mostly fresh melt water with low heat.

For reasons of numerical stability of the model, we force the water thickness within the vertical elements of the model in the grounding zone cavity to maintain a minimum $\epsilon$ of 5% of the cavity height at low tide, or 5 cm here (note not all the model element has to be filled with 100% water, which allows us to model seawater intrusion with a single vertical layer). This minimum layer is equivalent to a permanent layer of subglacial water at the glacier base, e.g., produced by basal friction and geothermal heat. In our simulations, we find that changing the minimum height of the water column to $\epsilon = 10\%$ of the height does not change the results at a significant level. The water is flushed in and out on a 12-hour cycle (Figure 2).

The plume of modeled meltwater ascends along the ice shelf base outside the cavity (Fig. 2c-d). A portion of this meltwater mixes with the surrounding more saline, warmer, sea water and intrudes the cavity again (Fig. 2e-f). About 70-80% of the water intrusion is seawater. Near the termination of the cavity, the water speed drops to zero as a result of the boundary condition. Ice melt also drops to zero. The transition occurs within 72% of the grounding zone width (Fig. S2).

*Sensitivity to the grounding zone width.* When we increase the grounding zone width, both the rate at which the cavity opens and the entrainment speed, $U_m$, increase. As a result, the modeled melt rate, cumulative melt rate, and integrated melt increase (Fig. 3). In the absence of curvature at the grounding zone entrance, we find that for every kilometer increase in grounding zone width, the mean melt rate increases by 60% and the integrated melt by 143%. When a small amount of curvature is introduced at the mouth of the grounding zone, the mean melt rate and integrated melt decrease by 10% compared to the case with no smoothing.

*Sensitivity to ocean thermal forcing.* As we increase ocean thermal forcing, the model predicts greater rates of ice melt within the grounding zone. For every 1°C increase in thermal forcing, the mean melt rate and total integrated melt increase by approximately 90%, i.e. almost linearly.

*Parameterization of melt.* We least square fit the simulated melt rate, $\dot{m}$, in meters per year in the form, $\dot{m} = AGZ^bTF^c$, where $A$ is a constant, $GZ$ is the grounding zone width in kilometers, $TF$ is thermal forcing at a depth of the grounding line, and $b$ and $c$ are constants. A similar formulation parameterizes the integrated melt rate, $\dot{M}$. In the absence of curvature, the optimal values for $A$, $b$, and $c$ for $\dot{m}$ are 0.03166, 0.5951, and 0.89, respectively. For $\dot{M}$, the coefficients are 0.0025, 1.433, and 0.882, respectively. If we introduce curvature at the grounding zone entrance, the parameters for $\dot{m}$ become A = 0.0111, b = 0.7043, and c = 0.882. For $\dot{M}$, they become A = 0.0008323, b = 1.55, and c = 0.882 for the integrated melt. The average and integrated melt rates, therefore, increase nearly linearly with ocean thermal forcing. The average melt rate exhibits a sublinear growth with the grounding zone width. The integrated melt exhibits a supra-linear

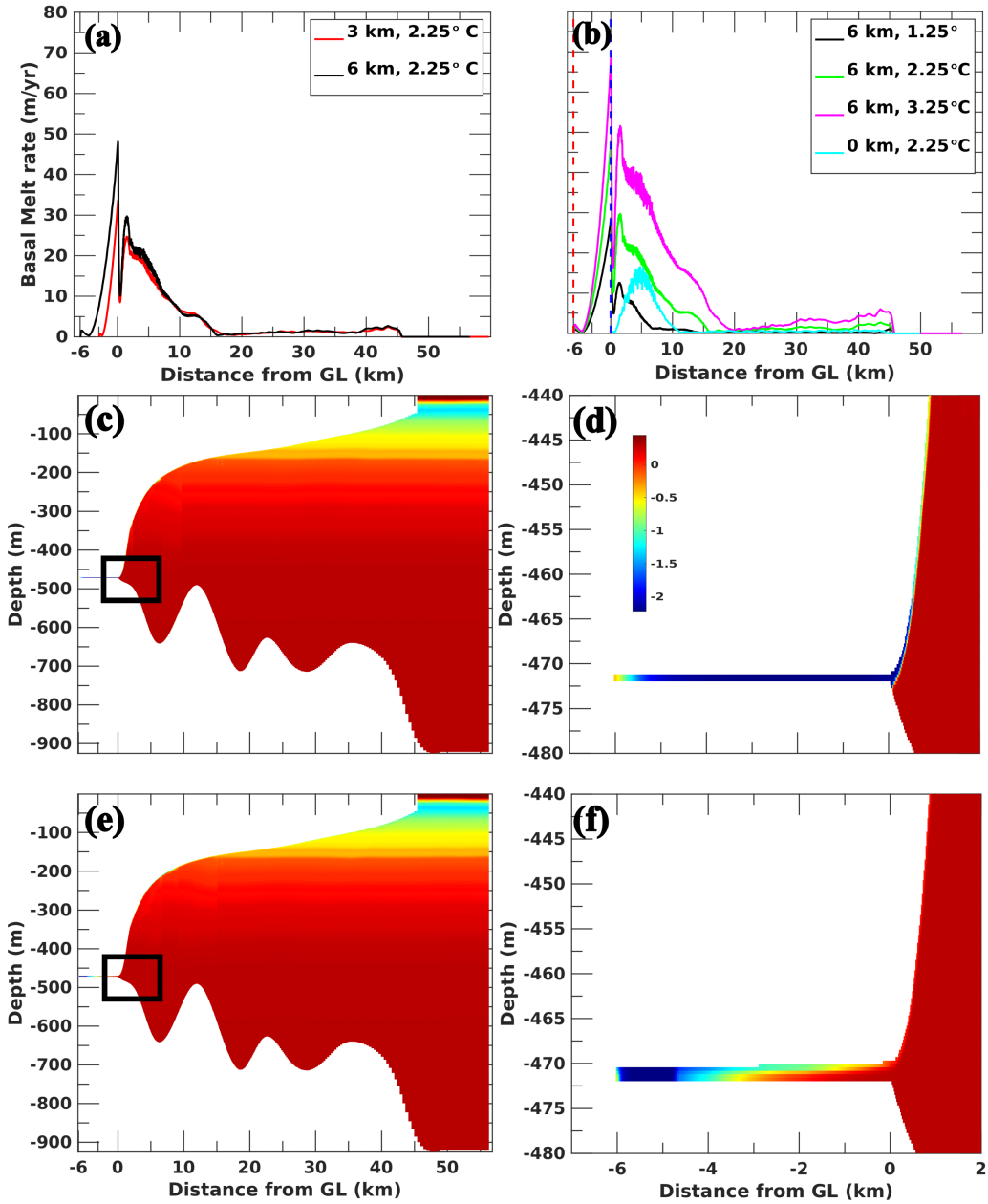


**Figure 2. Modeling of melt rates in the grounding zone of Petermann Glacier.** Average melt rate, $\dot{m}$, after one tidal cycle for (a) a 3-km and a 6-km wide grounding zone with 2.25°C thermal forcing and (b) a 6-km wide grounding zone with three thermal forcings and a fourth simulation with $TF = 2.25$°C and no grounding zone. Temperature snapshots after (c-d) 18 hours (low tide) and (e-f) 24 hours (high tide). (d) and (f) zoom on the grounding zone cavity (black rectangle) in (c) and (e).

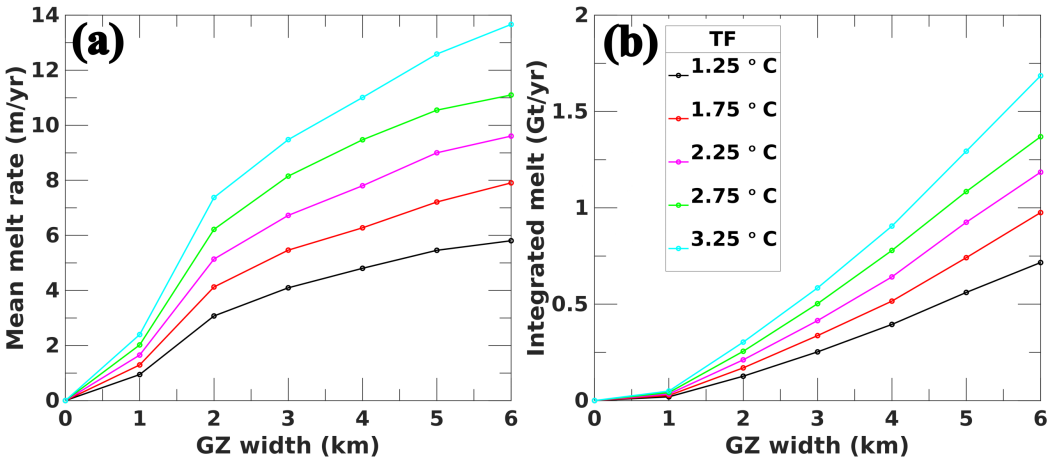


**Figure 3. Parameterization of the melt rate in the grounding zone of Petermann Glacier** for (a) averaged melt rate, $\dot{m}$, and (b) integrated melt, $\dot{M}$, as a function of the grounding zone (GZ) width and for different ocean thermal forcing, $TF$. Each diamond is one simulation, with a linear fit in between simulations. The model fit are $\dot{m} = 0.0111\ GZ^{0.704}\ TF^{0.882}$ and $\dot{M} = 0.0008323\ GZ^{1.55}\ TF^{0.882}$.

relationship with the grounding zone width since total melt is proportional to the length of the cavity.

## 4 Discussion

The model has a no-flow boundary condition at the upstream end of the grounding zone cavity. In the first tidal cycle, the melt rate is high at that upper boundary, then it converges to a lower value in the next iteration, and does not change after that (see Fig. S1). The simulations, therefore, reach a steady state quickly. There is no need to extend the simulations in time. The results are not affected by numerical instabilities.

The exponent coefficient for the grounding zone width, $b$, is less than 1, i.e. the melt is not increasing linearly with the cavity opening rate, which forces the speed of water flow, $U_m$. If the cavity was frictionless and infinite, the water should flow at the cavity opening rate and the coefficient $b$ should be unity. The sub-linear dependency is caused by water experiencing friction along the cavity walls, motion across density gradients, and slowing down to zero at the cavity termination. The lack of water flow at the termination of the cavity imposes zero melt. This region of no flow is a significant fraction of the cavity as it extends over 1-2 km for a 6-km long cavity (Fig. S2d).

In our simulation, we do not include subglacial discharge from the glacier. Subglacial discharge may have two opposing effects on the ice melt rates: 1) it may intensify the thermohaline circulation within the cavity by increasing the entrainment speed of the melt water plume during low tide; (2) conversely, it will oppose or block seawater inflow at high tide, thereby acting as a protective layer for the ice. Our minimum water height in the cavity is justified by the presence of subglacial water beneath the glacier produces a natural pathway to allow seawater intrusions (Warburton et al., 2020). Here, the model assumes a subglacial water layer of 5 cm with no input flow.

The geometry of the grounding zone influences the melt pattern and the location of the maximum melt rate. In the absence of high-resolution observations of the shape

of the grounding zone, i.e., ice shelf draft and bed topography, our modeling adopts an idealized rectangular cavity with smooth boundaries. The rationale for the smooth boundary is that high melt rates on sharp corners will naturally smooth them out. Most channels and ice shelf bases are smooth (Rignot & Steffen, 2008), except for basal crevasses.

Our findings indicate that the rate of ice melt is asymmetric during the tidal cycle (Fig. S2) as in (Warburton et al., 2020). When water enters the cavity, it leads to greater melting than when it exits the cavity. This disparity in melting is caused by the asymmetry in entrainment speed as $U_m$ has to drop to zero at the cavity termination. The water that exits the cavity consists mostly of meltwater, which has a lower thermal forcing and slower velocity. The melt water also encounters resistance as it moves against density gradients, leading to lower melt rates during the outflow. The asymmetry contributes to a sub-linear dependence of melt with the grounding zone width.

The distance of seawater intrusions is the maximum extent to which warm ambient water penetrates into the cavity within a tidal cycle. In our simulations, this distance is 72±3% of the cavity length (Fig. S2). It is, therefore, important for future studies to differentiate between the grounding zone width from the extent of seawater intrusions, i.e., recognize that the distance of intrusion of seawater will always be less than the grounding zone width. The model confirms that melt water is trapped in the cavity at low tide (Warburton et al., 2020). The distance of seawater intrusion does not change when we change the thermal forcing.

Differences in water density across the grounding zone region and ice shelf cavity will generate geostrophic currents. In addition, the Coriolis force at the scale of the fjord will intensify the melting of ice in the grounding zone differentially and re-distribute ocean heat laterally. We do not incorporate these effects in 2D, but it will be useful to incorporate them in 3D studies.

Increasing the number of vertical cells in the model within the cavity slightly reduces the peak melt rate at the cavity entrance (Fig. S3), but does not change the average and integrated melt rate significantly. This reduction occurs because, with more vertical layers, the melt water confined at the ice shelf base helps better insulate it from the underlying warm seawater. The extent of seawater intrusions remains unaffected. Here, we use a single vertical layer for the cavity to reduce computational complexity.

The modeled peak melt rates fall within the 40-80 m/yr range estimated from remote sensing data in the grounding zone (Ciraci et al., 2023). The values in Fig. 3 are cavity-averaged values, hence peak values are twice higher. With a thermal forcing $TF$ = 2.25°C, a cavity-averaged melt rate of 10 m/yr in the grounding zone, the total melt is 1.25 Gt/yr, which is 10% of the incoming glacier flux (about 12 Gt/yr). Within the flexure zone, the integrated melt is 3.5 Gt/yr or 30% of the glacier flux (Fig. S4). Overall, 40% of the ice melts away within the grounding and flexure zones combined.

If we assume that the waters in Petermann fjord warmed up by 0.33°C from 1.75°C to 2.25°C in recent years (Millan et al., 2022), the average melt rate in the 2-km grounding zone cavity must have increased by 2 m/yr (Fig. 3). If the model is correct, the ice shelf thinned by 40 m from 2000 to 2020. If we also include that the grounding zone width increased from 2 km in the late 1990s to 6 km in the 2020's, the average melt rate would have increased from 3 m/yr to 10 m/yr, for a total thinning of 140 m for 2000-2020. For comparison, estimates from remote sensing data report a maximum thinning of the cavity of 190 m at the center in 10 years and less on the sides (Ciraci et al., 2023). Hence, the combination of warmer water and greater seawater intrusions explains the observed thinning. The longer cavity increases melt more significantly than the warmer ocean temperature.

The ocean model confirms that kilometer-scale intrusions of seawater beneath grounded ice during the tidal cycle cause high rates of ice melt. The highest melt rates are recorded

at the mouth of the grounding zone. Because the loss of grounded ice directly affects basal resistance to flow, the melt rates in the grounding zone are critically important to glacier flow. Prior studies indicated that the inclusion of such melt rates would increase the glacier sensitivity to ocean warming and thereby increase the projections of sea level rise. We have now observational evidence for these intrusions and modeling evidence that these intrusions result in high melt rates.

## 5 Conclusions

We present the first 2D modeling of ice melt within the idealized grounding zone cavity of Petermann Glacier where remote sensing data indicate kilometer-size seawater intrusions beneath grounded ice at tidal frequencies. Using an ocean model, we predict a strong dependence of ice melt in the kilometer-size grounding zone cavity as a function of ocean thermal forcing and distance of seawater intrusions. We find that seawater intrusions operate efficient ice melt over 73% of the cavity, with no melt occurring at the termination of the cavity where melt water is trapped. The modeled melt rates are highest near the mouth of the cavity and higher than elsewhere in the ice shelf cavity. We present a parameterization of ice melt rates as a function of cavity length and ocean thermal forcing that will be relevant to ice sheet models. Ocean thermal forcing may be constrained by CTD data and ocean modeling. Cavity length may be constrained by InSAR observations or seawater intrusion modeling (Wilson et al., 2020). Future work shall examine the impact of a lateral re-distribution of ocean heat in 3D simulations, with more vertical elements, and how an active layer subglacial water beneath the glacier may affect the results. We recommend to obtain detailed in-situ observations of ice melt rates in the grounding zone given their critical role in glacier evolution.

## Open Research Section

The MITgcm model code is available at `https://doi.org/10.5281/zenodo.8208482`. Our MITgcm model setup, along with the modified ice shelf package, is available at `https://doi.org/10.5281/zenodo.8250817`. BedMachine Greenland is available at the National Snow and Ice Data Center (`https://doi.org/10.5067/GMEVBWFLWA7X`). The 2015 CTD data which we use is OD1507_10_CTD.txt and is available at Artic Data Center (`https://arcticdata.io/catalog/view/doi:10.18739/A2XS5JH16`).

### Acknowledgments

This work was conducted at the University of California Irvine and Caltech's Jet Propulsion Laboratory under a grant from NASA's Cryosphere Science Program.

## References

An, L., Rignot, E., Millan, R., Tinto, K., & Willis, J. (2019). Bathymetry of Northwest Greenland Using "Ocean Melting Greenland"(OMG) High-Resolution Airborne Gravity and other data. *Rem. Sens.*, *11*(2(11)), 131.

Brunt, K. M., Fricker, H. A., Padman, L., Scambos, T. A., & O'Neel, S. (2010). Mapping the grounding zone of the Ross Ice Shelf, Antarctica, using ICESat laser altimetry. *Ann. Glaciol.*, *51*(55), 71–79.

Cai, C., Rignot, E., Menemenlis, D., & Nakayama, Y. (2017). Observations and modeling of ocean-induced melt beneath Petermann Glacier Ice Shelf in northwestern Greenland. *Geophys. Res. Lett.*, *44*(16), 8396–8403.

Ciraci, E., Rignot, E., Scheuchl, B., Tolpekin, V., Wollersheim, M., An, L., ... Dini, L. (2023). Melt rates in the kilometer-size grounding zone of Petermann Glacier, Greenland, before and during a retreat. *Proc. Nat. Acad. Sci.*, *120*(20), e2220924120.

Dansereau, V., Heimbach, P., & Losch, M. (2014). Simulation of subice shelf melt rates in a general circulation model: Velocity-dependent transfer and the role of friction. *J. Geophys. Res.: Oceans*, *119*(3), 1765–1790.

Holland, D. M., & Jenkins, A. (1999). Modeling thermodynamic ice–ocean interactions at the base of an ice shelf. *J. Phys. Ocean.*, *29*(8), 1787–1800.

Jakobsson, M., Hogan, K., Mayer, L., Mix, A., Jennings, A., Stoner, J., ... C., S. (2018). The Holocene retreat dynamics and stability of Petermann Glacier in northwest Greenland. *Nature Comm.*, *9*, 2104.

Jenkins, A. (1991). A one-dimensional model of ice shelf-ocean interaction. *J. Geophys. Res.: Oceans*, *96*(C11), 20671–20677.

Johannessen, O. M., Babiker, M., & Miles, M. W. (2013). Unprecedented retreat in a 50-year observational record for Petermann Glacier, North Greenland. *Atmos. Ocean. Scie. Lett.*, *6*(5), 259–265.

Jordan, J., Holland, P., Goldberg, D., Snow, K., Arthern, R., Campin, J., ... Jenkins, A. (2018). Ocean-forced ice-shelf thinning in a synchronously coupled ice-ocean model. *J. Geophys. Res.: Oceans*, *123*(2), 864–882.

Losch, M. (2008). Modeling ice shelf cavities in az coordinate ocean general circulation model. *J. Geophys. Res.: Oceans*, *113*(C8).

Marshall, J., Adcroft, A., Hill, C., Perelman, L., & Heisey, C. (1997). A finite-volume, incompressible navier stokes model for studies of the ocean on parallel computers. *J. Geophys. Res.: Oceans*, *102*(C3), 5753–5766.

Millan, R., Mouginot, J., Derkacheva, A., Rignot, E., Milillo, P., Ciraci, E., ... Bjørk, A. (2022). Ongoing grounding line retreat and fracturation initiated at the Petermann Glacier ice shelf, Greenland after 2016. *The Cryosphere*, *16*, 3021-3031.

Mouginot, J., Rignot, E., Bjørk, A. A., Van den Broeke, M., Millan, R., Morlighem, M., ... Wood, M. (2019). Forty-six years of Greenland Ice Sheet mass balance from 1972 to 2018. *Proc. Nat. Academ. Sci.*, *116*(19), 9239–9244.

Münchow, A., Padman, L., & Fricker, H. A. (2014). Interannual changes of the floating ice shelf of Petermann Gletscher, North Greenland, from 2000 to 2012. *J. Glaciol.*, *60*(221), 489–499.

Nick, F., Luckman, A., Vieli, A., Van der Veen, C. J., Van As, D., Van De Wal, R., ... Floricioiu, D. (2012). The response of Petermann Glacier, Greenland, to large calving events, and its future stability in the context of atmospheric and oceanic warming. *J. Glaciol.*, *58*(208), 229–239.

Parizek, B., Christianson, K., Anandakrishnan, S., Alley, R., Walker, R., Edwards, R., ... others (2013). Dynamic (in) stability of Thwaites Glacier, West Antarctica. *J. Geophys. Res.: Earth Surface*, *118*(2), 638–655.

Reeh, N., Christensen, E. L., Mayer, C., & Olesen, O. B. (2003). Tidal bending of glaciers: a linear viscoelastic approach. *Ann. Glaciol*, *37*, 83-89.

Rignot, E., & Steffen, K. (2008). Channelized bottom melting and stability of floating ice shelves. *Geophys. Res. Lett.*, L02503.

Robel, A. A., Wilson, E., & Seroussi, H. (2022). Layered seawater intrusion and melt under grounded ice. *The Cryosphere*, *16*(2), 451–469.

Sayag, R., & Worster, M. G. (2013). Elastic dynamics and tidal migration of grounding lines modify subglacial lubrication and melting. *Geophys. Rese. Lett.*, *40*(22), 5877–5881.

Seroussi, H., & Morlighem, M. (2018). Representation of basal melting at the grounding line in ice flow models. *The Cryosphere*, *12*(10), 3085–3096.

Walker, R., Parizek, B., Alley, R., Anandakrishnan, S., Riverman, K., & Christianson, K. (2013). Ice-shelf tidal flexure and subglacial pressure variations. *Earth Planet. Sci. Lett.*, *361*, 422–428.

Warburton, K., Hewitt, D., & Neufeld, J. (2020). Tidal grounding-line migration modulated by subglacial hydrology. *Geophys. Res. Lett.*, *47*(17), e2020GL089088.

Wilson, E. A., Wells, A. J., Hewitt, I. J., & Cenedese, C. (2020). The dynamics of a subglacial salt wedge. *J. Fluid Mech.*, *895*, A20.